

Towards Topological Quasi-Freestanding Stanene via Substrate Engineering

Domenico Di Sante,¹ Philipp Eck,¹ Maximilian Bauernfeind,² Marius Will,²
Ronny Thomale,¹ Jörg Schäfer,² Ralph Claessen,² and Giorgio Sangiovanni¹

¹*Institut für Theoretische Physik und Astrophysik, Universität Würzburg,
Am Hubland Campus Süd, Würzburg 97074, Germany**

²*Physikalisches Institut and Röntgen Research Center for Complex Material Systems,
Universität Würzburg, Am Hubland Campus Süd, Würzburg 97074, Germany*

(Dated: December 14, 2024)

In search for a new generation of spintronics hardware, material candidates for room temperature quantum spin Hall effect (QSHE) have become a contemporary focus of investigation. Inspired by the original proposal for QSHE in graphene, several heterostructures have been synthesized, aiming at a hexagonal monolayer of heavier group IV elements in order to promote the QSHE bulk gap via increased spin-orbit coupling. So far, however, the monolayer/substrate coupling, which can manifest itself in strain, deformation, and hybridization, has proven to be detrimental to the aspired QSHE conditions for the monolayer. Specifically focusing on stanene, the Sn analogue of graphene, we investigate how an interposing buffer layer mediates between monolayer and substrate in order to optimize the QSHE setting. From a detailed density functional theory study, we highlight the principal mechanisms induced by such a buffer layer to accomplish quasi-free standing stanene in its QSHE phase. We complement our theoretical predictions by presenting the first real attempts to grow a buffer layer on SiC(0001) on which stanene can be deposited.

I. INTRODUCTION

Quantum spin Hall (QSH) systems are two-dimensional bulk non-conducting materials featuring topologically non-trivial conducting edge modes, whose stability against external perturbations is ensured by time reversal symmetry [1, 2]. After the first theoretical prediction in graphene by Kane and Mele [3, 4] and the subsequent prediction and experimental realization in HgTe/CdTe quantum wells [5, 6], it became evident that the small bulk energy gap represents the hardest obstacle to render QSH materials operative at room temperature, and as such relevant to technological applications.

The first obvious strategy to increase the bulk gap is to enhance the spin-orbit coupling strength of the constituting atoms. Within the group IV elements, freestanding honeycomb-like structures made by Si, Ge, and Sn atoms, dubbed silicene, germanene, and stanene, respectively, were estimated in theory to exhibit gaps up to 100 meV [7–9]. A realistic implementation, however, always requires the stabilization of freestanding 2D layers on a supporting substrate, with no guarantee that the resulting symmetry breaking keeps the QSH phase intact. For instance, this detrimental effect to the QSHE phase is seen when an insulating MoS₂ substrate stabilizes the growth of germanene [10] or a Bi₂Te₃ template is used to accommodate stanene flakes [11]. In both cases, the bulk topological gap does not survive the interaction with the substrate, and either yields a metallic or trivially insulating monolayer.

By contrast, a constructive effect of the substrate is observed for bismuthene on SiC [12]. There, the strong

hybridization between the substrate and the Bi π orbitals leaves a sizable topological bulk gap of 0.8 eV, highlighting bismuthene as the first material realization of a QSH system operable at ambient temperatures. Monolayer WTe₂ is another recent example where the interaction between the 2D layer and the substrate stabilizes the QSH phase by opening a finite gap, thus avoiding contributions from the bulk material which may be detrimental to the edge conductivity [13–15].

On the basis of this observations, it is evident that any proper theoretical investigation must properly take into consideration the role of substrates. With a particular focus on stanene, several studies have attempted to include these effects [11, 16–19], while only a few of them focus on technologically achievable, and hence relevant, substrates [18, 19]. The integration of the QSH physics into ambient life devices could the likeliest be achieved through the use of commercial wafers of wide-gap semiconductors serving as suitable substrates. SiC(0001) turns out to be a promising way along this direction [20]. However, dangling bonds passivation is a well-known problem of semiconductor surfaces. The presence of highly reactive surface charge may be detrimental to the QSH phase. Recent theory investigations usually proceed by removing the effect of the dangling bonds via hydrogen (H) saturation [18, 21]. Despite its modeling efficiency, this strategy cannot be considered a viable solution, since no evidence of a 2D material grown on a pure H-saturated surface has so far been reported in the literature.

In this article, we explore the possibility of realizing the QSH phase in stanene on SiC(0001) by insertion of a buffer layer of group-III and group-V elements. As the central positive impact, the valence electrons from the buffer atoms saturate the SiC dangling bonds. Still, this positive effect is counterbalanced by an unavoidable monolayer/substrate hybridization. For buckled geome-

*Electronic address: domenico.disante@physik.uni-wuerzburg.de

tries, as it is also the case for stanene, a concomitant staggered potential (Semenoff mass [22]) emerges, imposing a detrimental effect on the QSH formation [3]. Our strategy consists of limiting the quantitative effect of the Semenoff mass formation via a proper choice of the buffer characteristics. Although our DFT calculations show that on Al, Ga, In and Tl stanene is topologically trivial, our careful study of the group-III buffers helps to identify the mechanism behind the Semenoff mass generation. We then proceed by using this knowledge to predict that the detrimental effect of the Semenoff mass is efficiently minimized upon using elements of group V. Our calculations demonstrate that the topology in stanene can be comfortably stabilized for buffer layers made of P, As, and Sb atoms, by which we hope to stimulate further experimental progress along this direction.

II. METHODS

For our theoretical study of stanene on buffered SiC(0001) we employed state-of-the-art first-principles calculations based on the density functional theory as implemented in the Vienna ab initio simulation package (VASP) [23], within the projector-augmented-plane-wave (PAW) method [24, 25]. The generalized gradient approximation as parametrized by the PBE-GGA functional for the exchange-correlation potential was used [26], by expanding the Kohn-Sham wavefunctions into plane-waves up to an energy cut-off of 600 eV. We sampled the Brillouin zone on an $8 \times 8 \times 1$ regular mesh, and when considered, spin-orbit coupling (SOC) was self-consistently included [27]. The stanene low-energy models are extracted by projecting onto Sn p_z - and sp_2 -like maximally localized Wannier functions (MLWF) by using the WANNIER90 package [28], and we compute the \mathbb{Z}_2 topological invariant following the general method of Soluyanov and Vanderbilt [29].

Each atom from group III and V can saturate three dangling bonds from the SiC surface, either from Si atoms of the Si-terminated SiC or from C atoms from the C-terminated SiC, as shown in Fig. 1b). This saturation strategy requires a minimal $\sqrt{3} \times \sqrt{3}R(30^\circ)$ reconstruction, whose Brillouin zone and crystal structure are reported in Fig. 1a). Moreover, a 2×2 hexagonal lattice of stanene ($a = 9.28\text{\AA}$) turns out to have a good commensuration with a 3×3 reconstruction of SiC (lateral compressive strain $\varepsilon \sim 0.62\%$), suggesting a promising strain-free overlayer deposition. A 3×3 buffered SiC template ultimately shows at its surface a triangular lattice of buffer atoms (see Fig. 1c).

The large structural reconstructions enforce a folding of the electronic states into the supercell Brillouin zones, which map onto the primitive 1×1 Brillouin zones as sketched in Fig. 1a). It is usually simpler to achieve a transparent physical description in the latter setting, where the unfolded bandstructure readily compares with the freestanding models when the symmetry breaking in-

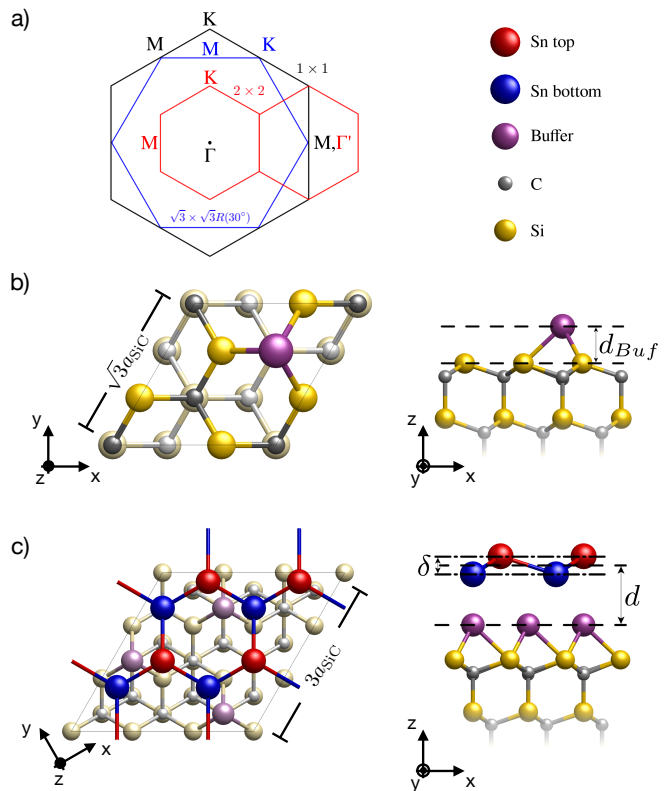


FIG. 1: a) Brillouin zones of $\sqrt{3} \times \sqrt{3}R(30^\circ)$ SiC (blue), 1×1 stanene (black) and 2×2 stanene (red), with relative high symmetry points. b) Top and side views of the crystalline structure of buffered $\sqrt{3} \times \sqrt{3}R(30^\circ)$ SiC and c) 2×2 stanene/ 3×3 buffered SiC. The bottom termination of the slab models is artificially passivated by H atoms. In the top view in panel c) the colors of the substrate are intentionally less intense compared to panel b) in order to emphasize the hexagonal lattice of 2×2 stanene.

duced by the reconstruction is weak. The unfolding procedure we adopt in this work follows the lines described in Refs 30, 31.

For the experimental realization of a buffer layer we use n -doped (0.01-0.03 Ωcm) Si-terminated 4H-SiC(0001) wafer pieces. For the preparation of an atomically smooth, well-ordered substrate surface on large-scales, the wafer pieces undergo a dry-etching process in a helium diluted hydrogen atmosphere with a flow of 2 standard litre per minute at 950 mbar and temperatures around 1200 $^\circ\text{C}$ for roughly 10 minutes. Subsequently, the H-terminated SiC(0001) samples [21] were transferred to the preparation chamber (base pressure $p < 3 \times 10^{-11}$ mbar) using a vacuum suitcase. Surface quality was inspected in situ by low-energy electron diffraction (LEED).

Prior to the epitaxial growth of Al, the H termination of SiC(0001) has to be removed. This is achieved by heating the substrate to $\sim 620^\circ\text{C}$ with a subsequent cooling to $\sim 350^\circ\text{C}$ in the Al beam of the effusion cell, to form the Al- $(\sqrt{3} \times \sqrt{3})$ lattice, as shown in Fig. 2, where

LEED clearly shows the reconstruction of the commensurate buffer layer. All samples were heated by direct current and the temperatures were measured pyrometrically.

III. GROUP-III BUFFER LAYERS

Atoms from the group III of the periodic table, i.e., Al, Ga, In and, Tl all share the same s^2p^1 valence electronic configuration. It is well-known that Al and other group III atoms can saturate the (111) surface of a silicon crystal, inducing a $\sqrt{3} \times \sqrt{3}R(30^\circ)$ reconstruction [32–35]. The underlying mechanism is that the three Al valence orbitals saturate three of the Si surface dangling bonds, which naturally leads to a $\sqrt{3} \times \sqrt{3}$ coverage of the Si substrate. By analogy, and based on the similarities that the SiC electronic structure shares with Si, we indeed assume here that deposition of group III atoms induces on the SiC surface the same $\sqrt{3} \times \sqrt{3}R(30^\circ)$ reconstruction as on silicon. Our theoretical assumption is indeed experimentally proven here for the first time for the case of an Al buffer on SiC. Fig. 2 shows a clear $\sqrt{3} \times \sqrt{3}R(30^\circ)$ reconstruction (red arrows) on an underlying 1×1 template (blue arrows).

When an atom of group III is adsorbed on the SiC surface, its three valence electrons saturate the SiC dangling bonds by forming three sp^3 -like bonding states. The fourth orbital of the sp^3 combination, empty and with sp_z -like character, makes an antibonding in-gap state. The resulting band structures for this type of buffer layers on SiC (Si-face) are shown in Fig. 3a). The energy position of the in-gap antibonding state anticorrelates with the bonding distance of the buffer atom to SiC, as we show in Fig. 3b). The lighter the buffer atom the

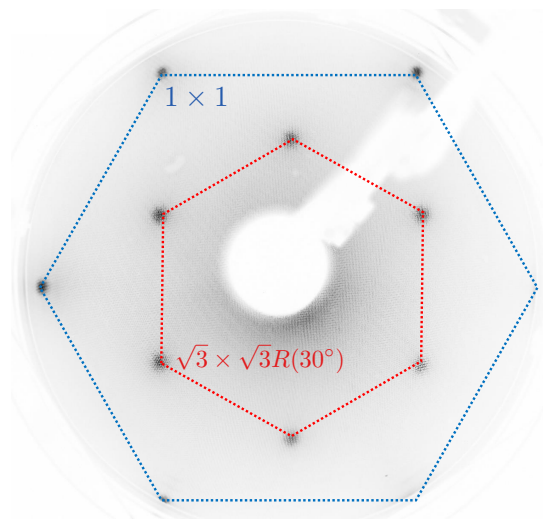


FIG. 2: LEED image of $\text{Al}-(\sqrt{3} \times \sqrt{3})R30^\circ$ on Si-terminated 4H-SiC(0001) recorded with an electron energy of 40 eV. Arrows in red and blue highlight the Al induced $(\sqrt{3} \times \sqrt{3})$ and (1×1) spots, respectively.

shorter is the resulting distance, with the concomitant upward level repulsion of the antibonding orbital. This anticorrelation trend is independent of the SiC termination, holding both for the Si- and for the C-terminated surface.

The energy position of the antibonding level, and in turn the excitation gap, affects the strength of the hybridization when the stanene monolayer is deposited. A small gap results in sizable hybridization effects between the buffer and stanene leading to a significant distinction between the top and bottom Sn atoms of the buckled geometry. The induced Semenoff mass is detrimental to the QSH phase since it tends to compete with the second-nearest neighbor spin-orbit coupling (SOC) [3].

To gain more insights into the physical mechanisms behind the interaction between stanene and the buffered substrate, we focus on the specific case of Al/SiC. We monitor the evolution of the electronic band structure of stanene as its bonding distance is artificially tuned from an unrealistically large value down to the equilibrium one $d_{\text{eq}} \sim 2.9 \text{ \AA}$ (see Fig. 4a). The 2×2 structure reconstruction induced by the lattice commensuration leads to band foldings [30]. However, when the stanene-substrate distance is large enough to reduce the hybridization effects and the Coulomb interaction, we recover the freestanding stanene electronic properties. By unfolding the stanene band structure from the 2×2 Brillouin zone into the primitive 1×1 , we can directly compare with the results of the freestanding description [8]. The reduction of the distance towards the equilibrium geometry and the concomitant interaction causes the opening of hybridization gaps in the stanene band structure. At the same time

TABLE I: Summary of the DFT results we obtained for buffer layers made of group III elements (for relaxed geometry). Si and C refer to the silicon and carbon terminated SiC, respectively. ΔE_K is the stanene energy gap at the K point. The dash symbol indicates that the system is metallic. d_{Buf} , d and δ are the buffer layer-SiC distance, the stanene-buffer distance and the buckling height, respectively. \mathbb{Z}_2 is the topological invariant.

	Al	Ga	In	Tl
Si				
ΔE_K (meV)	56	66	60	63
d_{Buf} (\AA)	1.7	1.8	2.0	2.2
d (\AA)	2.9	2.9	3.0	3.1
δ (\AA)	0.44	0.48	0.48	0.48
\mathbb{Z}_2	0	0	0	0
C				
ΔE_K (meV)	-	-	-	-
d_{Buf} (\AA)	1.3	1.4	1.8	2.1
d (\AA)	2.8	2.8	3.0	3.1
δ (\AA)	0.44	0.48	0.48	0.48
\mathbb{Z}_2	-	-	-	-

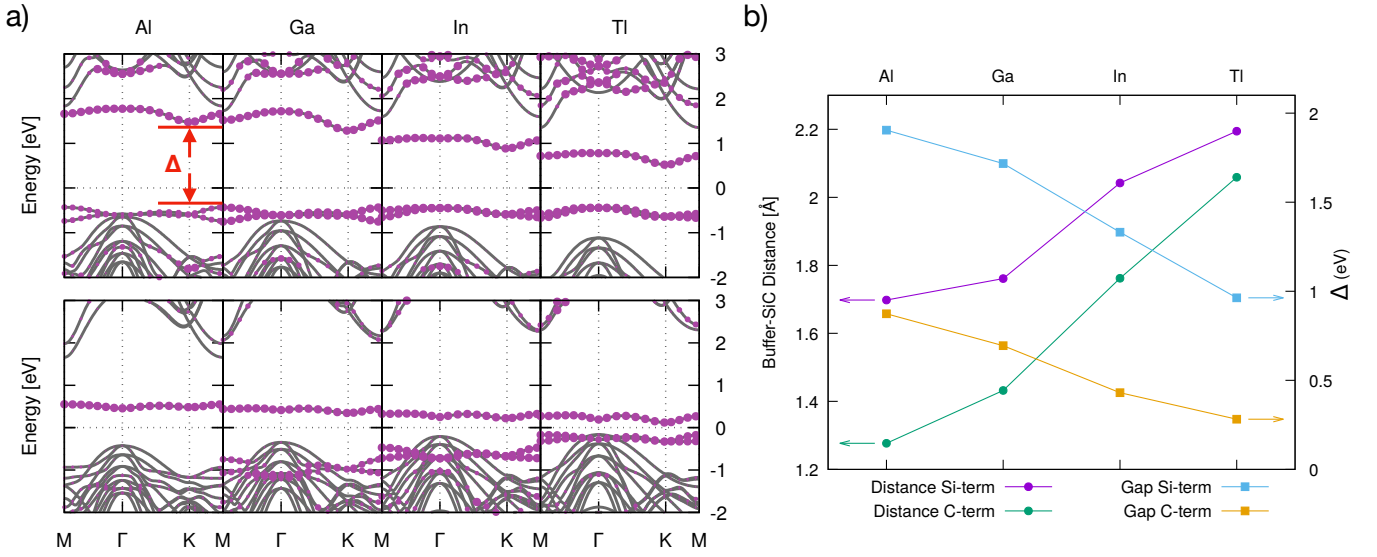


FIG. 3: a) Electronic band structures for group III buffered SiC (top row for Si-face and bottom row for C-face SiC) along the high-symmetry lines of the $\sqrt{3} \times \sqrt{3}R(30^\circ)$ Brillouin zone (see Fig. 1a). The coloured dot highlight the orbital contribution from the buffer atom. b) Anticorrelation of the bonding-antibonding states gap with the distance between the group-III atom buffer layer and the SiC surface, shown for both substrate terminations (Si- and C-faces).

we see a distribution (spread) of stanene character over the Al/SiC electronic states. When the distance becomes smaller than the critical value $d_{cr} \sim 3.2\text{\AA}$, we observe a sudden change of the \mathbb{Z}_2 topological invariant from 1 to 0 (Fig. 4b). This evidence marks the transition from a freestanding-like topologically non-trivial to a topologically trivial stanene and demonstrates that stanene on Al/SiC is a trivial insulator. As we will see, the same mechanism leads to a different conclusion in the case of group V.

A change in the topological invariant can only occur through an inversion of the bulk gap [1, 2]. This evolution is indeed what we observe and show in Fig. 4c. First of all, we observe that the breaking of the inversion symmetry induced by the presence of the substrate removes the band degeneracies at the K points. This effect goes under the name of valley-contrasting physics, or valleytronics, and is a well-known property of gated graphene and transition metal dichalcogenides [36, 37]. The gap closure is accompanied by a change in the sublattice character of the bands. Actually, in the topological (trivial) phase, the contribution from the bottom Sn (top Sn) atom dominates the valence band maximum, and vice-versa for the conduction band minimum. The closure of the gap occurs through a linear Dirac-like band touching where the sublattice character is equally mixed, as highlighted by the brownish color of the linear branches in the middle panel of Fig. 4c.

In the next Section, we will establish an analogy with the topological transition as described by the Kane and Mele model [3], and analyze the quantitative role of the Semenoff mass. However, before concluding, we want to state that the trend observed here for stanene on Al/SiC

is common to all the group-III buffer setups, regardless of the SiC termination (see Table I). The fact that the heaviest buffer atoms lead to trivial groundstates as well can be inferred by noting that Al/SiC shows the largest bulk gap (see Fig. 3b). From this analysis, it is clear that a significant Semenoff mass suppression can only be achieved if the buffer antibonding level is entirely removed from the gap.

After a general paragraph on the Semenoff mass term, we will discuss how the conclusions reached for group III will turn from unfavourable to favourable regarding the topology in the case of group-V buffers.

IV. THE ROLE OF THE SEMENOFF MASS

In this section we give a rundown of the fundamental aspects of the Kane and Mele model [3]. Then we establish the link with the topological transition we observed in stanene. The tight-binding Hamiltonian reads

$$\begin{aligned}
 H = & t \sum_{\langle ij \rangle, \alpha} c_{i, \alpha}^\dagger c_{j, \alpha} + i\lambda_{\text{SO}} \sum_{\langle\langle ij \rangle\rangle, \alpha\alpha'} \nu_{ij} c_{i, \alpha}^\dagger s_{\alpha\alpha'}^z c_{j, \alpha'} \\
 & + i\lambda_R \sum_{\langle ij \rangle, \alpha\alpha'} c_{i, \alpha}^\dagger (\mathbf{s} \times \hat{\mathbf{d}}_{ij})_{\alpha\alpha'}^z c_{j, \alpha'} \\
 & + \lambda_v \sum_{i, \alpha} \xi_i c_{i, \alpha}^\dagger c_{i, \alpha}
 \end{aligned} \quad (1)$$

where the first is a nearest neighbor hopping term on the honeycomb lattice and the second a mirror symmetric SOC one (here $\nu_{ij} \hat{\mathbf{u}}_z = (2/\sqrt{3})(\hat{\mathbf{d}}_1 \times \hat{\mathbf{d}}_2)$ where $\hat{\mathbf{d}}_{1,2}$ are unit vectors along the two bonds from site j to site i , and

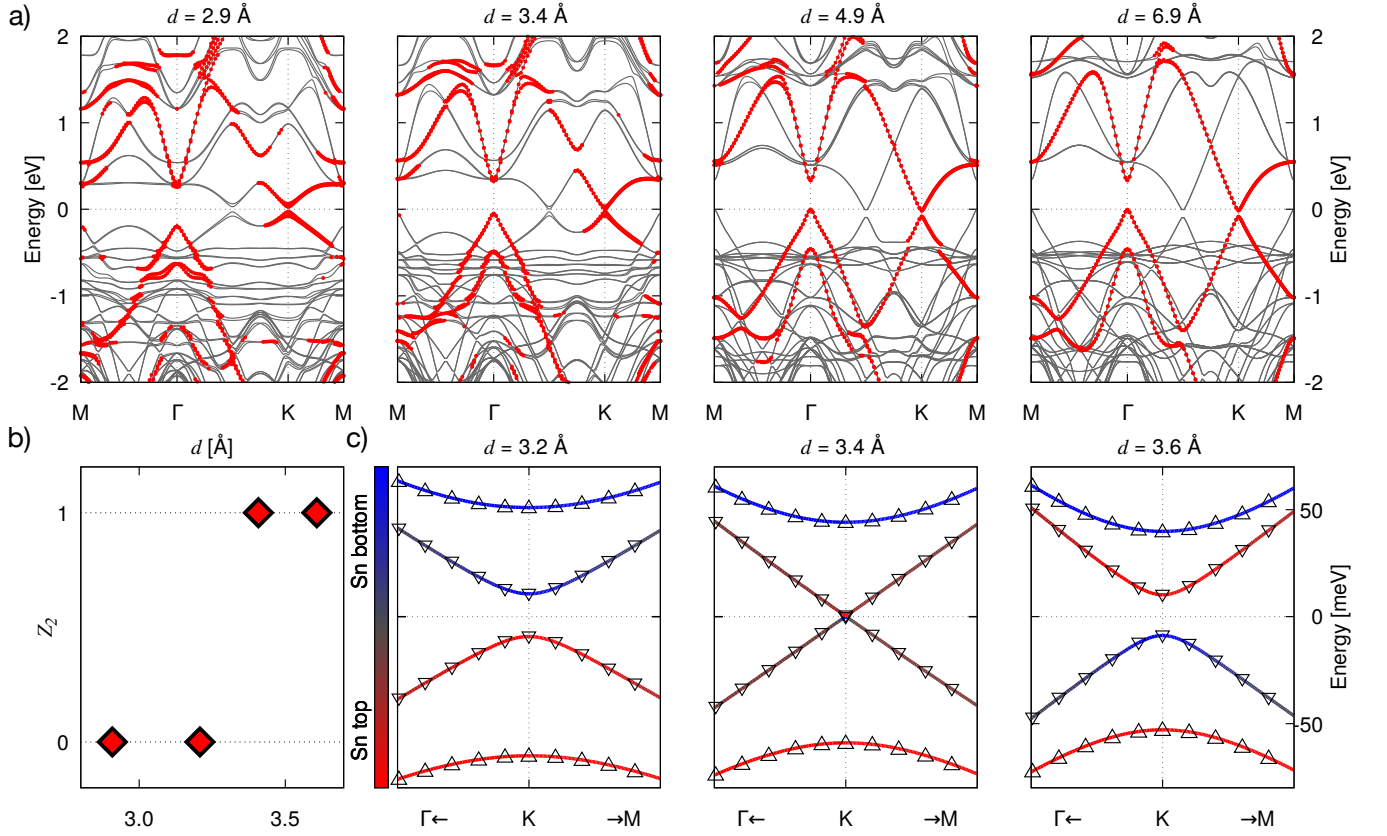


FIG. 4: a) Evolution of the stanene/Al/SiC electronic band structure at different stanene-Al buffer distances ($d = 2.9 \text{ \AA}$, 3.4 \AA , 4.9 \AA and 6.9 \AA from left to right panels). Red dots highlight the unfolding weight from the 2×2 Brillouin zone onto the primitive 1×1 . b) Behaviour of the Z_2 topological invariant close to the critical transition distance d_{cr} . c) Zooms around the K point across the topological transition. Red and blue colors refer to orbital character from top and bottom Sn atoms, respectively.

$\hat{\mathbf{u}}_z$ is a unit vector perpendicular to the stanene plane), and \mathbf{s} are the Pauli matrices for the electron spin. The third term is a nearest-neighbor Rashba coupling due to a perpendicular electric field or to an interaction with a substrate and the last term sets the staggered potential (Semenoff mass) λ_v ($\xi_i = \pm 1$ depending on the sublattice). The latter differentiates the on-site energies of the two atoms constituting the bipartite honeycomb lattice. If one neglects the Rashba part in (1), the momentum-space Hamiltonian assumes the form

$$H(\mathbf{k}) = t(1 + 2 \cos x \cos y)\Gamma_1 - 2t \cos x \sin y \Gamma^{12} + \lambda_{\text{SO}}(2 \sin 2x - 4 \sin x \cos y)\Gamma^{15} + \lambda_v \Gamma_2 \quad (2)$$

with $x = k_x a/2$ and $y = \sqrt{3}k_y a/2$ (a being the hexagonal unit cell lattice constant, i.e. $\langle ij \rangle = a/\sqrt{3}$), $\Gamma_1 = \sigma_x \otimes s_0$, $\Gamma_2 = \sigma_z \otimes s_0$ and $\Gamma_5 = \sigma_y \otimes s_z$ three of the five Dirac matrices with σ_i describing the sublattice degree of freedom and $\Gamma^{ab} = [\Gamma_a, \Gamma_b]/2i$. At the K point, the Hamiltonian is diagonal in the sublattice basis $A\uparrow, B\uparrow, A\downarrow, B\downarrow$:

$$\begin{bmatrix} \lambda_v - 3\sqrt{3}\lambda_{\text{SO}} & 0 & 0 & 0 \\ 0 & -(\lambda_v - 3\sqrt{3}\lambda_{\text{SO}}) & 0 & 0 \\ 0 & 0 & \lambda_v + 3\sqrt{3}\lambda_{\text{SO}} & 0 \\ 0 & 0 & 0 & -(\lambda_v + 3\sqrt{3}\lambda_{\text{SO}}) \end{bmatrix}$$

The two \uparrow - and the two \downarrow -eigenvalues with smaller and larger splitting, respectively, give perfect account of the four bands visible in the actual DFT calculation (Fig. 4c). The matching between the DFT result and the Kane-Mele model can be pushed further upon comparing the sublattice character of these four eigenvalues and its evolution with d . We define $d = d_{\text{cr}}$ as the distance at which the two lowest-lying DFT eigenvalues touch each other. For $d < d_{\text{cr}}$ the character of both the uppermost eigenvalues is on one sublattice, namely the one corresponding to the bottom Sn-atom, while both eigenvalues in valence band belong to the top Sn. For $d > d_{\text{cr}}$ the sublattice character at the K point is instead interchanged, a situation which in the mapping onto the Kane-Mele is obtained in the QSH phase for values of the Semenoff mass $\lambda_v < 3\sqrt{3}\lambda_{\text{SO}}$ [3]. In the topological phase with inverted sublattice character, the lattice site with the highest on-site energy ($+\lambda_v$) contributes thus to the valence band maximum at the K point, at odds with the trivial atomic limit.

Let us note that the inversion of sublattice character is well defined only at the K and K' points, where the Kane-Mele Hamiltonian is diagonal in the original basis. A

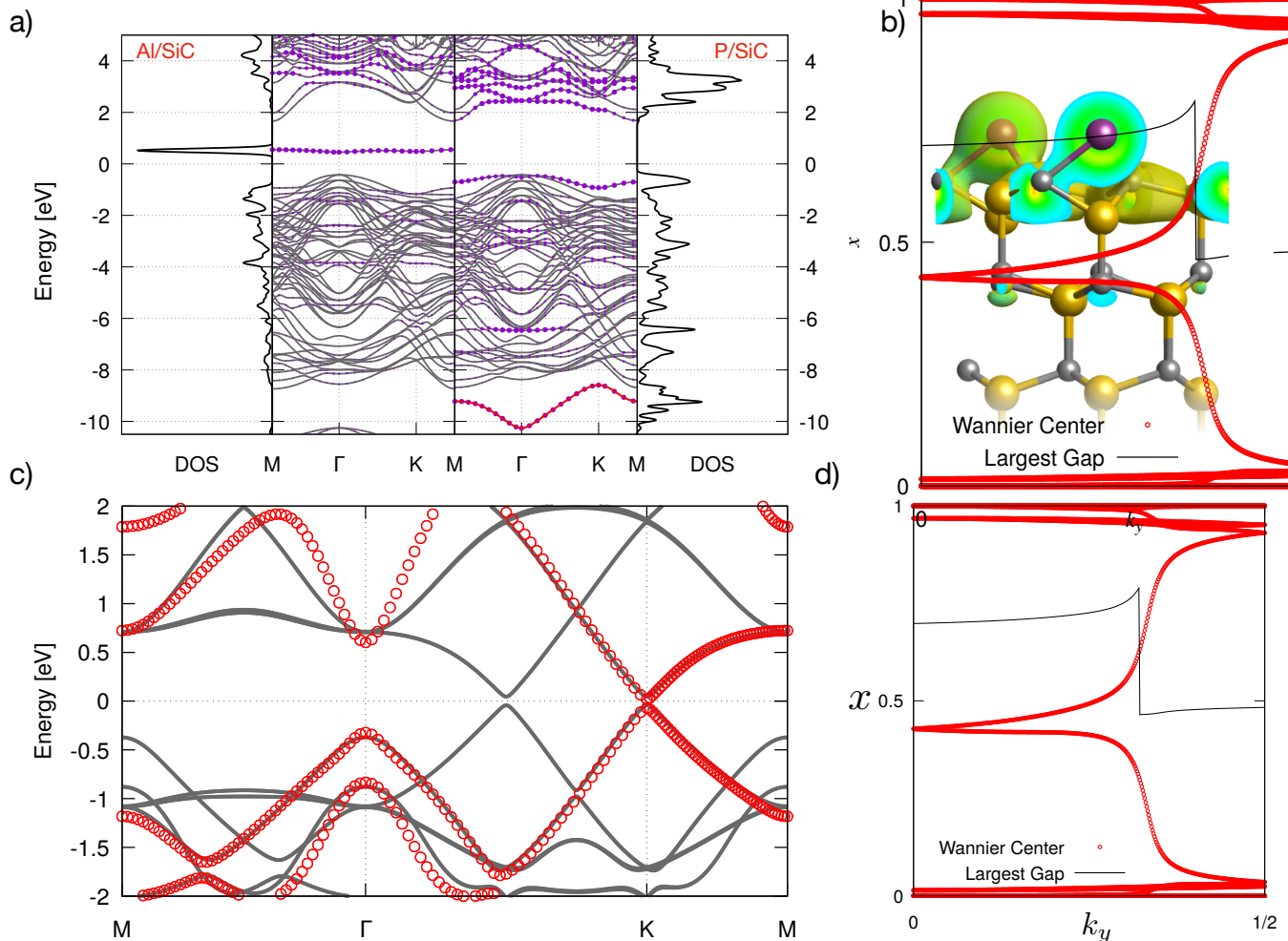


FIG. 5: a) Buffer resolved density of the states and bandstructure of Al/SiC and P/SiC (C-face hereafter in this caption), respectively. The dots in the bandstructure highlight the orbital weight of buffer atoms for P/SiC. b) Charge distribution projected on the states forming the lone pair around 10 eV of binding energy for P/SiC. c) Bandstructure of 2×2 stanene on P/SiC with the red dots referring to freestanding stanene in the primitive 1×1 structure. d) Evolution of the Wannier charge centers (WCCs, x in units of 2π) as a function of the pumping parameter k_y for stanene on P/SiC (red symbols) and track of the middle of the largest gap between two consecutive WCCs (black line). The sudden jump is the typical fingerprint of a $\mathbb{Z}_2 = 1$ topological groundstate.

suitable definition of the character over the whole BZ can be obtained by rotating the Kane-Mele Hamiltonian at each k -point in the basis of the eigenvectors of (2) calculated at $\lambda_{\text{SO}} = 0$. At the Γ point, for instance, the Kane-Mele model is made of two identical 2×2 blocks, with $\pm\lambda_v$ on the diagonal and $3t$ between the A and B sites. Going away from the Γ point and continuing to use the “bonding”-“antibonding” basis defined above, the SOC acquires off-diagonal elements which mix the “bonding”-“antibonding” eigenvectors approaching K and K’ leading to the inversion at the topological phase transition.

So far we have discussed the qualitative correspondence between the Kane-Mele model and the DFT results. Now, we make a more quantitative comparison by estimating the Semenoff mass term via a projection of the DFT band structure onto localized atomic orbitals [28].

At d_{eq} we extract a difference between the p_z onsite energies of the top- and bottom-Sn atoms of $2\lambda_v = 0.23$ eV. The highest levels belong to the bottom Sn-atoms, that feel the buffer layer stronger than the top ones and are hence pushed up in energy. The estimate of λ_{SO} from the Wannier projection is less straightforward than for λ_v . In the Kane-Mele Hamiltonian λ_{SO} represents a non-local term which accounts for the coupling of orbitals with parallel spin on the same sublattice. However, a finite buckling angle introduces a non-vanishing local contribution to the SOC [38]. By assuming that the final value of λ_{SO} is only marginally affected by the interaction with the substrate, we can estimate following the procedure of Ref. 38 that in stanene $3\sqrt{3}\lambda_{\text{SO}} \sim 64$ meV. It turns out that the relationship $\lambda_v > 3\sqrt{3}\lambda_{\text{SO}}$ holds for stanene on the Al buffer at the equilibrium distance, confirming the

trivial groundstate found in our DFT computations.

Let us briefly comment on the quantitative estimate of the Semenoff mass: we extract the staggered potential from the different of the p_z -local levels of the two sublattices. This is however done within a Wannier projection of the DFT band-structure onto a model containing all the p -orbitals of Tin as well as orbitals from the buffer atoms. This means that our Wannier Hamiltonian is defined on a much larger Hilbert space than the one of the Kane-Mele model, which assumes one single orbital per site. In order to directly connect to λ_v we would have hence to further downfold our Wannier Hamiltonian onto a p_z -like only low-energy model. A direct projection onto such a minimal model turned however out to yield quite poor matching with the DFT bands. Furthermore, there is another reason why we work with an extended local basis set, namely that this allows us to disentangle hybridization effects coming from the buffer.

In the previous analysis we neglected the Rashba coupling in Eq. 1. The presence of a finite λ_R mixes the \uparrow - and \downarrow -blocks of the Hamiltonian breaking the conservation of the z -component of the spin. Moreover, a spin-texture appears around the K point. However, we checked that this effect is negligible, proving that our assumption $\lambda_R = 0$ is justified and does not affect the qualitative arguments given above.

V. GROUP-V BUFFER LAYERS

Equipped with the microscopic understanding gained in the previous section of the mechanism responsible for the topological transition in stanene on the buffer layer, we can now address the key question of our study: how to realize quasi free-standing topologically non-trivial stanene. The obvious goal is to reduce the Semenoff mass and our analysis of the group-III buffer discloses to us

TABLE II: Same as Table I but for buffer layers made of group-V elements. The column on the left refers to Si-face or C-face of the SiC substrate.

	P	As	Sb	Bi
Si				
ΔE_K (meV)	68	43	40	61
d_{Buf} (\AA)	1.8	1.9	2.2	2.3
d (\AA)	3.2	3.5	3.6	3.6
δ (\AA)	0.46	0.45	0.46	0.46
\mathbb{Z}_2	0	0	0	0
C				
ΔE_K (meV)	69	55	42	11
d_{Buf} (\AA)	1.3	1.4	1.6	1.8
d (\AA)	3.9	3.8	3.9	3.7
δ (\AA)	0.44	0.44	0.44	0.45
\mathbb{Z}_2	1	1	1	0

the successful strategy for that. This is to saturate the bonds responsible for the in-gap state which, in the case of group III, destructively hybridizes with stanene. Two more valence electrons would exactly serve the purpose and the two additional ones made available by group-V atoms in their p -shell offer us the solution.

In Fig. 5a) we compare the density of the states (DOS) and bandstructures of Al/SiC and P/SiC (C-face). From the comparison between group-III and V buffer it is clear that our expectation of the quenching of the antibonding state is fulfilled: for group V we indeed observe a chemically inert lone pair characterized by a pronounced s -type orbital character (see Fig. 5b). This is located around 10 eV below the Fermi level, leaving as a consequence more “room” within the gap for an interference-free positioning of the stanene layer. Thanks to the reduced monolayer/substrate interaction the induced Semenoff mass is indeed smaller. This is illustrated in Table II, where we summarize our results for stanene on group-V buffer/SiC substrates.

The bandstructure of stanene on C-terminated P/SiC is shown in Fig. 5c). It is clear how this resembles to a large extent the one of freestanding stanene [8]. Such conclusion is further confirmed by the explicit computation of the \mathbb{Z}_2 invariant (see Fig. 5d), where a Kramers’ pair switching indicates the non-trivial topological nature ($\mathbb{Z}_2 = 1$) [29].

Our calculations reveal therefore that P, As and Sb buffer atoms on C-terminated SiC are ideal templates to host stanene in the QSH phase. On the other hand, stanene on Bi/SiC is a trivial insulator right at the verge of the topological transition, even though it is likely that Bi on SiC prefers the 2/3 coverage, as recently reported in the case of bismuthene/SiC [12]. Moreover, all the configurations we studied on the Si-terminated SiC are trivial insulators. We ascribe this result to the larger electronegativity of C over Si. Being less electronegative, Si attracts less negative charge from the buffer atoms compared to what C does, resulting in turn in a larger SiC buffer distance (see Fig. 3b). This is an indication that the charge around the buffer atoms can be more easily transferred to stanene, spoiling the robustness of the QSH phase.

VI. CONCLUSIONS

Through a systematic first-principles analysis we have unveiled the mechanisms underlying the delicate QSH formation in stanene grown on a SiC(0001) substrate, and how these growth conditions can be crucially improved by an appropriate buffer between substrate and monolayer. Starting from the guiding principle that a technologically relevant substrate is crucial for any future integration of QSH systems in novel spin-based devices, which as such highlights SiC as one of the most promising substrate candidates, we have accomplished a substrate engineering mechanism that employs a buffer

layer for the saturation of the substrate dangling bonds. We have further revealed the microscopic processes that are detrimental to the topological phase formation due to the electronic hybridization between the substrate and the stanene monolayer. Combining these insights, we predict a stable QSH phase of stanene in three cases of group-V buffered SiC.

By analyzing the hybridization between the stanene layer and the buffer, and by mapping the full ab initio Hamiltonian onto a generalized effective Hamiltonian including a staggered potential (Semenoff mass term), we show that some buffer layers are more suitable than others to protect the QSH formation in the monolayer. The strategy we follow then is to minimize the detrimental staggered potential by choosing such atoms which have their bonding and antibonding states energetically far away from the chemical potential. This leads us to concrete suggestions for promising buffer materials, in particular the use of group-V elements (P, As, Sb).

Note that our theoretical study only establishes a lower bound to the potential range of parameter space in which the QSH phase in stanene might be stabilized by proper substrate engineering. This is because our DFT approach utilizes the GGA approximation, which, due to the prohibitive size of the reconstructions we considered, would be extremely time-consuming to overcome by alternative

procedures. The use of GGA suggests that a $\sim 20\%$ underestimation of the antibonding states energy position is possible (see Fig. 3a), and that some of the trivial configurations we have found (Table I and II) are in fact still QSH domain. In terms of an explicit analysis of the buffer-assisted growth of stanene on SiC, we reported for the first time a clear LEED pattern (Fig. 2) demonstrating a $\sqrt{3} \times \sqrt{3}R(30^\circ)$ reconstruction of SiC after Al deposition. Together, our efforts represent the first promising steps towards the accomplishment of the buffer engineering concept which is the central motif of our work.

Acknowledgement

The authors acknowledge G. Profeta for fruitful and inspiring discussions. This work was supported by the DFG through SFB1170 "Tocotronics" and by ERC-StG-336012-Thomale-TOPOLECTRICS. We gratefully acknowledge the Gauss Centre for Supercomputing e.V. (www.gauss-centre.eu) for funding this project by providing computing time on the GCS Supercomputer SuperMUC at Leibniz Supercomputing Centre (www.lrz.de).

-
- [1] M. Z. Hasan and C. L. Kane, *Colloquium: Topological insulators*, Rev. Mod. Phys. **82**, 3045 (2010).
- [2] X.-L. Qi and S.-C. Zhang, *Topological insulators and superconductors*, Rev. Mod. Phys. **83**, 1057 (2011).
- [3] C. L. Kane and E. J. Mele, Z_2 , Phys. Rev. Lett. **95**, 146802 (2005).
- [4] C. L. Kane and E. J. Mele, *Quantum Spin Hall Effect in Graphene*, Phys. Rev. Lett. **95**, 226801 (2005).
- [5] B. A. Bernevig, T. L. Hughes, and S.-C. Zhang, *Quantum Spin Hall Effect and Topological Phase Transition in HgTe Quantum Wells*, Science **314**, 1757 (2006).
- [6] M. König, S. Wiedmann, C. Brüne, A. Roth, H. Buhmann, L. W. Molenkamp, X.-L. Qi, and S.-C. Zhang, *Quantum Spin Hall Insulator State in HgTe Quantum Wells*, Science **318**, 766 (2007).
- [7] A. Molle, J. Goldberger, M. Houssa, Y. Xu, S.-C. Zhang, and D. Akinwande, *Buckled two-dimensional Xene sheets*, Nature Materials **16**, 163 (2017).
- [8] Y. Xu, B. Yan, H.-J. Zhang, J. Wang, G. Xu, P. Tang, W. Duan, and S.-C. Zhang, *Large-Gap Quantum Spin Hall Insulators in Tin Films*, Phys. Rev. Lett. **111**, 136804 (2013).
- [9] F. Geissler, J. C. Budich, and B. Trauzettel, *Group theoretical and topological analysis of the quantum spin hall effect in silicene*, New Journal of Physics **15**, 085030 (2013).
- [10] L. Zhang, P. Bampoulis, A. N. Rudenko, Q. Yao, A. van Houselt, B. Poelsema, M. I. Katsnelson, and H. J. W. Zandvliet, *Structural and Electronic Properties of Germanene on MoS₂*, Phys. Rev. Lett. **116**, 256804 (2016).
- [11] F.-F. Zhu, W.-J. Chen, Y. Xu, C.-L. Gao, D.-D. Guan, C.-H. Liu, D. Qian, S.-C. Zhang, and J.-F. Jia, *Epitaxial growth of two-dimensional stanene*, Nature Materials **14**, 1020 (2015).
- [12] F. Reis, G. Li, L. Dudy, M. Bauernfeind, S. Glass, W. Hanke, R. Thomale, J. Schäfer, and R. Claessen, *Bismuthene on a SiC substrate: A candidate for a high-temperature quantum spin Hall material*, Science **357**, 287 (2017).
- [13] X. Qian, J. Liu, L. Fu, and J. Li, *Quantum spin Hall effect in two-dimensional transition metal dichalcogenides*, Science **346**, 1344 (2014).
- [14] S. Tang, C. Zhang, D. Wong, Z. Pedramrazi, H.-Z. Tsai, C. Jia, B. Moritz, M. Claassen, H. Ryu, S. Kahn, J. Jiang, H. Yan, M. Hashimoto, D. Lu, R. G. Moore, C.-C. Hwang, C. Hwang, Z. Hussain, Y. Chen, M. M. Ugeda, Z. Liu, X. Xie, T. P. Devereaux, M. F. Crommie, S.-K. Mo, and Z.-X. Shen, *Quantum spin Hall state in monolayer WTe₂*, Nat. Phys. **13**, 683 (2017).
- [15] S. Ok, L. Muechler, D. Di Sante, G. Sangiovanni, T. Neupert, and R. Thomale, *Electronic structure of the topological insulator monolayer WTe₂*, (to be published).
- [16] C.-Z. Xu, Y.-H. Chan, P. Chen, X. Wang, D. Flötotto, J. A. Hlevyack, G. Bian, S.-K. Mo, M.-Y. Chou, and T.-C. Chiang, *Gapped electronic structure of epitaxial stanene on InSb(111)*, Phys. Rev. B **97**, 035122 (2018).
- [17] Z. Ni, E. Minamitani, Y. Ando, and S. Watanabe, *Germanene and stanene on two-dimensional substrates: Dirac cone and Z_2 invariant*, Phys. Rev. B **96**, 075427 (2017).
- [18] F. Matusalem, F. Bechstedt, M. Marques, and L. K. Teles, *Quantum spin Hall phase in stanene-derived over-*

- layers on passivated SiC substrates, *Phys. Rev. B* **94**, 241403 (2016).
- [19] F. Matusalem, D. S. Koda, F. Bechstedt, M. Marques, and L. K. Teles, *Deposition of topological silicene, germanene and stanene on graphene-covered SiC substrates*, *Scientific Reports* **7**, 15700 (2017).
- [20] S. Glass, G. Li, F. Adler, J. Aulbach, A. Fleszar, R. Thomale, W. Hanke, R. Claessen, and J. Schäfer, *Triangular Spin-Orbit-Coupled Lattice with Strong Coulomb Correlations: Sn Atoms on a SiC(0001) Substrate*, *Phys. Rev. Lett.* **114**, 247602 (2015).
- [21] S. Glass, F. Reis, M. Bauernfeind, J. Aulbach, M. R. Scholz, F. Adler, L. Dudy, G. Li, R. Claessen, and J. Schfer, *Atomic-Scale Mapping of Layer-by-Layer Hydrogen Etching and Passivation of SiC(0001) Substrates*, *The Journal of Physical Chemistry C* **120**, 10361 (2016).
- [22] G. W. Semenoff, *Condensed-Matter Simulation of a Three-Dimensional Anomaly*, *Phys. Rev. Lett.* **53**, 2449 (1984).
- [23] G. Kresse and J. Furthmüller, *Efficient iterative schemes for ab initio total-energy calculations using a plane-wave basis set*, *Phys. Rev. B* **54**, 11169 (1996).
- [24] G. Kresse and D. Joubert, *From ultrasoft pseudopotentials to the projector augmented-wave method*, *Phys. Rev. B* **59**, 1758 (1999).
- [25] P. E. Blöchl, *Projector augmented-wave method*, *Phys. Rev. B* **50**, 17953 (1994).
- [26] J. P. Perdew, K. Burke, and M. Ernzerhof, *Generalized Gradient Approximation Made Simple*, *Phys. Rev. Lett.* **77**, 3865 (1996).
- [27] S. Steiner, S. Khmelevskyi, M. Marsmann, and G. Kresse, *Calculation of the magnetic anisotropy with projected-augmented-wave methodology and the case study of disordered Fe_{1-x}Co_x alloys*, *Phys. Rev. B* **93**, 224425 (2016).
- [28] A. A. Mostofi, J. R. Yates, Y.-S. Lee, I. Souza, D. Vanderbilt, and N. Marzari, *Wannier90: A Tool for Obtaining Maximally-Localised Wannier Functions*, *Comput. Phys. Commun.* **178**, 685 (2008).
- [29] A. A. Soluyanov and D. Vanderbilt, *Computing topological invariants without inversion symmetry*, *Phys. Rev. B* **83**, 235401 (2011).
- [30] W. Ku, T. Berlijn, and C.-C. Lee, *Unfolding First-Principles Band Structures*, *Phys. Rev. Lett.* **104**, 216401 (2010).
- [31] M. Tomić, H. O. Jeschke, and R. Valentí, *Unfolding of electronic structure through induced representations of space groups: Application to Fe-based superconductors*, *Phys. Rev. B* **90**, 195121 (2014).
- [32] J. Lander and J. Morrison, *Surface reactions of silicon with aluminum and with indium*, *Surf. Sci.* **2**, 553 (1964).
- [33] J. E. Northrup, *Si(111) $\sqrt{3} \times \sqrt{3}$ -Al: An Adatom-Induced Reconstruction*, *Phys. Rev. Lett.* **53**, 683 (1984).
- [34] J. M. Nicholls, B. Reihl, and J. E. Northrup, *Unoccupied surface states revealing the Si(111) $\sqrt{3} \times \sqrt{3}$ -Al, -Ga, and -In adatom geometries*, *Phys. Rev. B* **35**, 4137 (1987).
- [35] R. J. Hamers, *Effects of coverage on the geometry and electronic structure of Al overlayers on Si(111)*, *Phys. Rev. B* **40**, 1657 (1989).
- [36] D. Xiao, W. Yao, and Q. Niu, *Valley-Contrasting Physics in Graphene: Magnetic Moment and Topological Transport*, *Phys. Rev. Lett.* **99**, 236809 (2007).
- [37] D. Xiao, G.-B. Liu, W. Feng, X. Xu, and W. Yao, *Coupled Spin and Valley Physics in Monolayers of MoS₂ and Other Group-VI Dichalcogenides*, *Phys. Rev. Lett.* **108**, 196802 (2012).
- [38] C.-C. Liu, H. Jiang, and Y. Yao, *Low-energy effective Hamiltonian involving spin-orbit coupling in silicene and two-dimensional germanium and tin*, *Phys. Rev. B* **84**, 195430 (2011).